ChemElectroChem

Chemistry Europe
European Chemical Societies Publishing
ChemElectroChem

RESEARCH ARTICLE OPEN ACCESS

N,N'-Dialkylated Oxo-Verdazyl Radicals as Bipolar Organic Molecules for Symmetric Redox Flow Batteries

Elena S. Horst[1] | Karin Sowa[2,3] | Lena Lezius[1] | Nick Fehlings[3] | Constantin Daniliuc[1] | Sascha Nowak[3] | Mariano Grünebaum[2] | Martin Winter[2,3] | Armido Studer[1]

[1]Organisch-Chemisches Institut, Universität Münster, Münster, Germany | [2]Helmholtz Institute Münster IMD-4, Forschungszentrum Jülich GmbH, Münster, Germany | [3]MEET Battery Research Center, University of Münster, Münster, Germany

Correspondence: Mariano Grünebaum (m.gruenebaum@fz-juelich.de) | Martin Winter (martin.winter@uni-muenster.de) | Armido Studer (studer@uni-muenster.de)

Received: 23 December 2025 | **Revised:** 20 February 2026 | **Accepted:** 21 February 2026

Keywords: bipolar molecule | cyclic voltammetry | electrochemistry | radicals | verdazyl radical

ABSTRACT

The bipolar electrochemical properties of verdazyl radicals have long been known, and recently their application in symmetric redox flow batteries was investigated. However, the performance of aryl-substituted Kuhn- and oxo-verdazyl radicals in cycling experiments was unsatisfactory. In this work, *N,N'*-dialkylated oxo-verdazyl radicals were investigated as bipolar redox-active organic molecules (ROM). With a higher theoretical cell voltage than that of Kuhn- and arylated oxo-verdazyl radicals, these stable radicals revealed themselves a promising candidate for battery application. The initial tests of an *N,N'*-diisopropyl-verdazyl radical showed moderate cycling, stability and the formation of a new redox-active species during the cycling between neutral and cationic states was observed. By postcycling analysis, the decomposition product could be identified as the radical lacking an isopropyl group. By subsequent molecular engineering, the performance of the *N,N'*-dialkylated verdazyl radical could be improved by suppressing the decomposition pathway through variation of the N-substituent. Overall, the optimized verdazyl radical possesses a theoretical cell voltage of greater than 1.6 V. H-cell cycling experiments over 200 cycles showed an average Coulombic efficiency of 99.5% and a capacity fade of less than 0.1%/cycle for both oxidation and reduction. Finally, the best-performing oxo-verdazyl radicals were investigated under flow conditions.

1 | Introduction

The transition to a climate-neutral planet is one of the most pressing challenges of our society. To reach this goal while securing a sufficient energy supply, different technological solutions are being explored. Besides removing the produced greenhouse gases using negative emission technologies (NETs) [1], a central approach is replacing carbon-intensive fuel sources with renewable ones, such as wind and solar energies [2]. To ensure the reliable integration of these intermittent energy sources into our energy grid, the development of efficient energy storage systems is essential [3]. For stationary, large-scale applications, redox flow batteries (RFBs) represent a valuable solution to practical energy storage [4]. In particular, organic RFBs are highly promising along those lines. Operating in nonaqueous media provides a much wider electrochemical stability window compared to aqueous systems, and employing organic energy storage materials opens the door to using renewable or waste derived feedstocks for synthesis. However, a significant challenge faced by these systems is the crossover of active materials through the membrane into the opposing electrolyte. This crossover leads to a loss of active material and contamination of the opposite electrolyte, reducing the performance and lifetime of the battery.

Beyond optimization of membranes for organic systems [5, 6] or oligomerization of the redox-active material [7, 8], using the same redox-active organic molecules (ROM) as an anolyte and a catholyte represents a strategy to mitigate this problem [9].

Building the battery in a symmetric fashion not only facilitates the manufacturing of the battery but also reduces the chemical gradient across the membrane in the discharged state. The superior performance of symmetric RFBs compared to asymmetric systems has also been experimentally proven [9]. Moreover, a symmetric cell setup is more tolerant versus polarity reversals, which can lead to a longer battery lifetime [10].

To facilitate the fabrication of symmetric organic RFBs, stable organic radicals are a commonly utilized class of compounds [11, 12]. In contrast to nonradical ROMs, the presence of a singly occupied molecular orbital (SOMO) in radical ROMs allows both reduction and oxidation to produce nonradical, and potentially more stable, charged states. One of the most prominent stable nitroxide radicals in the context of battery research is the TEMPO radical. However, the high basicity of the TEMPO anion makes its application as a bipolar ROM cumbersome, and to date TEMPO has only been successfully cycled in H-cells at elevated temperatures using highly viscous ionic liquids [13]. Along with nitroxide radicals [14, 15], stable N-centered radicals have also been employed as bipolar ROMs. In contrast to nitroxide radicals (e.g., TEMPO), most N-centered radicals possess highly tunable properties based on minor structural changes [16]. In a symmetric battery setup, the first example was the Kuhn verdazyl radical studied by Dyker et al. in 2019 (Figure 1A). When utilized in a coin cell, the radicals showed limited cycling stability, retaining only 31% of the theoretical capacity after 50 cycles [17]. In 2023, Otten and coworkers investigated the same system in more detail. Their studies were conducted using an H-cell, resulting in a capacity retention of 55% after 71 cycles [18]. Postcycling analysis revealed the formation of a decomposition product during cycling due to stability issues of the radical in its neutral state. As the decomposition product did not demonstrate any reversible redox properties, it caused a noticeable capacity decay over time. 1 year after Dyker's initial report, our group studied the oxo-verdazyl analog in RFBs (Figure 1B) [19]. While the cell voltage increased, the cycling stability could not be improved compared to the previously studied Kuhn verdazyl radicals. Later in 2022, Otten et al. investigated Blatter radicals as bipolar ROMs for symmetric RFBs (Figure 1C) [20]. Substituent modification could improve the stability of the redox-flow system, maintaining 98% capacity after 100 cycles in an RFB while the theoretical cell voltage remains low at 1.12 V.

In 2005, Brook and coworkers successfully synthesized *N*,*N*'-diisopropyl oxo-verdazyl radicals [21], which were later electrochemically characterized by Hicks et al. [22]. The electron-rich nature of the alkyl-substituted radical facilitated the oxidation while rendering the reduction more challenging, leading to negatively shifted oxidation and reduction potentials. As the impact of the substitution pattern on the reduction potential seems to be more pronounced, the theoretical cell voltage of a flow battery could be increased by switching from aryl to alkyl substituents. Herein, *N*,*N*'-dialkylated verdazyl radicals will be electrochemically characterized and investigated in galvanostatic cycling experiments [23]. H-cell cycling will provide insights into degradation pathways, and molecular engineering should lead to an improved performance of the final ROM. The modular synthesis developed by Hicks et al. will give access to a variety of verdazyl radicals by just switching the used ketone and aldehyde in the synthesis. To better understand its potential in RFBs, the most promising verdazyl radical will be investigated during charge–discharge cycling in a modified GEN-2-Flow cell developed by Brushett and coworkers [24].

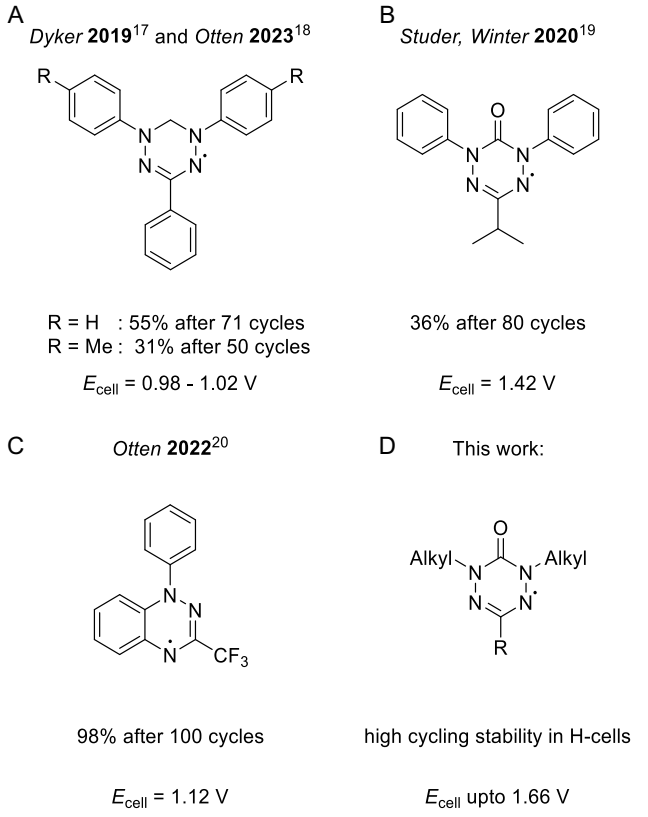

FIGURE 1 | Stable N-centered radicals as bipolar molecules for symmetric RBFs.

2 | Results and Discussion

2.1 | Initial Electrochemical Characterization and Long-Term Cycling Experiments of V-(*i*Pr)$_2$-Ph

Following the synthesis developed by Brook and coworkers, we prepared the verdazyl radical V-(*i*Pr)$_2$-Ph as a model compound for initial studies [21]. Cyclic voltammetry in 0.1 M $TBAPF_6$/CH_3CN confirmed its bipolar reversible redox behavior, with a reversible oxidation at $E_{ox}^{1/2}$ = +0.1 V and reduction at $E_{red}^{1/2}$ = −1.40 V versus $Fc|Fc^+$, resulting in an overall theoretical cell voltage (E_{cell}) of 1.5 V. Stationary H-cell experiments using a three-electrode setup were conducted to separately gain information regarding the electrochemical stability of the verdazyl oxidation and reduction steps during charge/discharge cycles. The investigated redox states are shown in Figure 2. The cycling experiments were performed using 2.5 mM **V-(*i*Pr)$_2$-Ph** in 0.1 M $TBAPF_6/CH_3CN$ and a constant current of 2 mA over 200

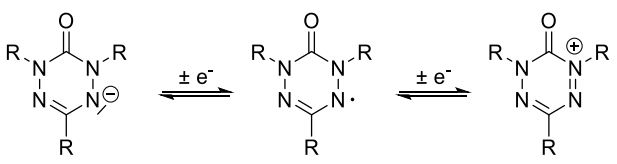

FIGURE 2 | Chemical structures of the verdazyl radical in its anionic, radical, and cationic states.

charge/discharge cycles. **V-(iPr)$_2$-Ph** initially shows moderate cycling stability between the neutral and the reduced state, retaining 76% capacity after 100 cycles and 52% after 200 cycles. The cycling data obtained under oxidative conditions delivered similarly satisfactory results, with the system retaining 81% of its initial capacity after 100 cycles and 75% after 200 cycles. Both the reduction and oxidation processes demonstrated an excellent average Coulombic efficiency of 99.5%.

At first glance, these results appear promising, suggesting superior long-term stability compared to the previously studied verdazyl radicals. However, a closer examination of the data obtained during oxidation revealed continuous potential changes during charging, as illustrated in Figure 3B. Notably, a new plateau appeared at a lower potential, ≈0.2 V below the original charging event. This suggests that during cycling, the verdazyl radical undergoes a decomposition, forming a new species that can still be reversibly oxidized, albeit at a lower potential. However, this species still participates in the cycling process, and, consequently, the decomposition does not impact the overall battery capacity. Nevertheless, its presence leads to a reduced cell voltage and ultimately results in an asymmetric cell configuration.

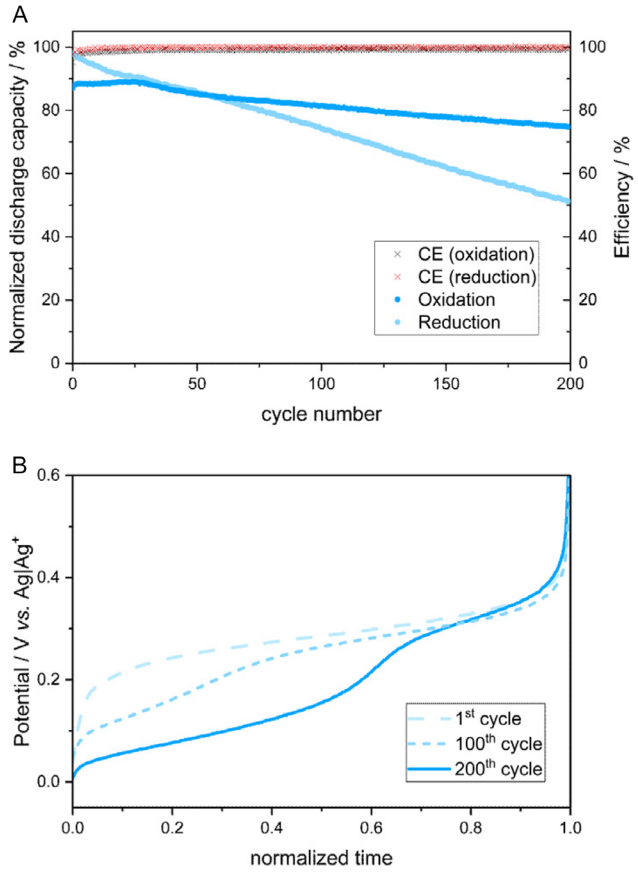

FIGURE 3 | Initial results of the H-cell cycling of **V-(iPr)$_2$-Ph** at a constant current of 2 mA (electrolyte solution consisted of 2.5 mM **V-(iPr)$_2$-Ph** and 0.1 M $TBAPF_6$ in MeCN). A: normalized discharge capacity to the initial charging cycle and CE versus cycle number for oxidation and reduction. B: potential versus time normalized against the total charging duration of the first, 100th, and last charging events during oxidative cycling.

2.2 | Investigation of Electrochemical Decomposition of V-(iPr)$_2$-Ph During Oxidative Cycling

Encouraged by the overall positive performance of **V-(iPr)$_2$-Ph**, we sought to identify the electrochemical decomposition products of **V-(iPr)$_2$-Ph** to improve long-term cell performance through judicious molecular design. Since the decomposition of the reductive cycling seems to be more complex (see SI for details), the studies will focus on the decomposition during oxidative cycling. Therefore, the residual solution after 200 cycles between verdazyl radical and its cation was chemically analyzed. Thin-layer chromatography (TLC) revealed a mixture of the verdazyl radical alongside a newly formed species (see SI for details). Mass spectroscopic (MS) analysis of the TLC spots identified this new species as a mono-dealkylated verdazyl derivative. By repeating the electrochemical cycling on a larger scale, we successfully isolated the dealkylated compound by column chromatography. The formation of the dealkylated decomposition product was confirmed through X-ray diffraction and NMR analysis [25]. To gain deeper insights into the nature of the decomposition process, the headspace of the working electrode side of the H-cell was analyzed after oxidation-controlled cycling. Using GC–MS, evidence of propene formation during redox cycling was found (Figure 4B). Based on these observations, we propose that upon oxidation the heterocyclic core is transformed into a good leaving group that facilitates a Hofmann-type elimination of an isopropyl group as propene (Figure 4A). The lack of such decomposition products after reductive cycling further supports the hypothesis of the oxidized verdazyl radical being the origin for the decomposition. Moreover, as one equivalent of protons is released during this process, we suggest the existence of an equilibrium between the protonated and deprotonated species. To identify the electroactive species taking part in the cycling, the isolated decomposition product was electrochemically characterized using cyclic voltammetry (Figure 4C).

The cyclic voltammogram showed a reversible reduction at −1.0 V versus Fc|Fc$^+$, which appears at too low a potential to be the redox process experimentally observed in the oxidation-controlled H-cell cycling experiment. To check whether the protonated decomposition product could be the active species, trifluoroacetic acid (TFA) was added. Indeed, a reversible redox process resulted at the expected potential of −0.1 V versus Fc|Fc$^+$, indicating that the protonated decomposition product is the active species in the cycling experiment. To clarify which nitrogen atom is protonated, DFT calculations were conducted, showing that protonation of N5 is favored over N4 by 5.7 kcal/mol. The protonated species (see Figure 4A) resembles an oxidized, mono-H-substituted verdazyl radical **V-(iPr,H)-Ph**, whose electrochemical stability is assumed to be comparable to that of the initial verdazyl radical. It has to be noted that similar decomposition products were isolated under oxidative conditions for less stable methylated and benzylated oxo-verdazyl radicals [26, 27].

2.3 | Improving Molecular Design of the Oxo-Verdazyl Radicals

Following identification of the decomposition product formed during oxidative cycling of **V-(iPr)$_2$-Ph**, verdazyl radicals with

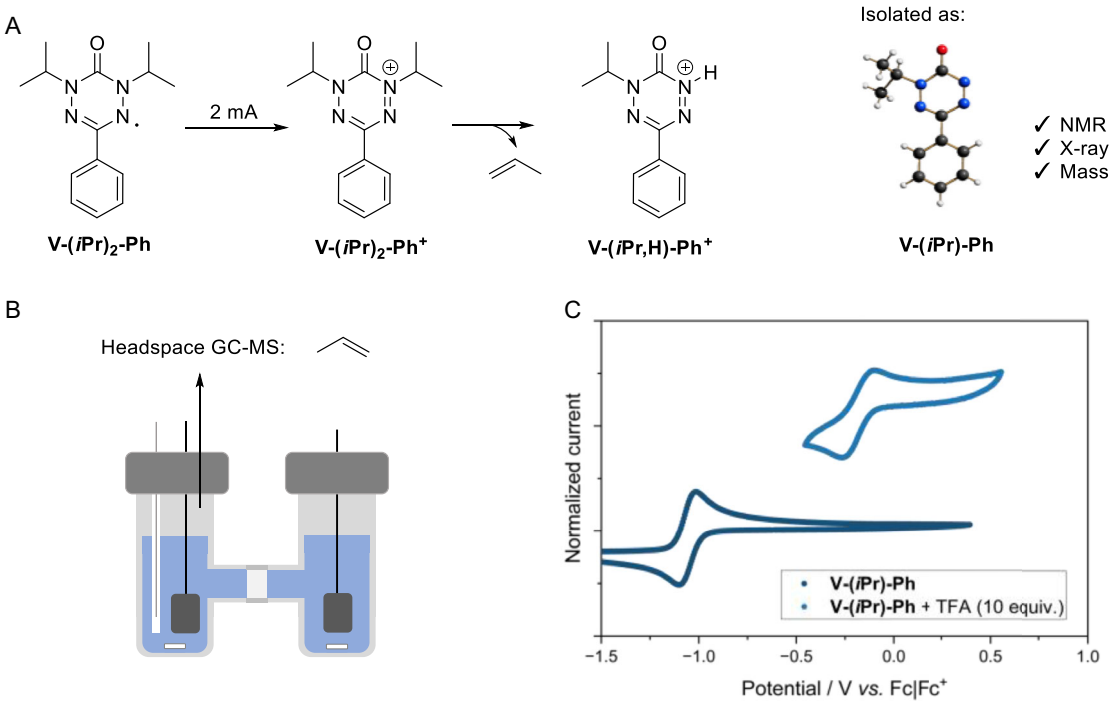

FIGURE 4 | (A) Proposed decomposition pathway during oxidative cycling of **V-(*i*Pr)$_2$-Ph**. (B) Schematic representation of the H-cell. (C) Cyclic voltammetry measurement of the isolated decomposition product in MeCN/TBAPF$_6$ with and without added TFA. For the measurement, a glassy carbon micro disk as a working electrode, a nonaqueous reference electrode and a Pt-coil as a counter electrode were used (Setup described in the SI).

different substitution patterns were synthesized, and their performance as a catholyte was investigated. Along these lines, we studied the aryl-substituted verdazyl radical **V-(Ph)$_2$-Ph**, where the formation of a similar decomposition product should be fully suppressed. To disfavor an alkenyl fragmentation in *N*, *N*'-dialkyl-verdazyl radicals upon oxidation, cyclohexyl groups were considered (see **V-(Cy)$_2$-Ph**) carrying fewer β-C–H protons accompanied with a more restricted conformational space. Furthermore, the expected analog alkenes elimination would lead to the formation of cyclohexenes and thus circumvent the problem of gas evolution. By varying the C-substituent, the influence of the localization of the positive charge was examined. Due to the more electron-rich nature of **V-(Cy)$_2$-*p*OMePh**, the positive charge is presumed to be more delocalized, which should further suppress N-dealkenylation during oxidative cycling. Moreover, verdazyls carrying cyclic N-substituents with high ring strain, such as cyclopentyl and cyclobutyl groups were investigated. Unfortunately, in both cases, isolation under air led to decomposition of the radical. However, exclusion of air during the work-up gave access to radical **V-(c4)$_2$-Ph** (see SI for details). All N-alkylated verdazyl radicals were synthesized according to the same synthetic procedure. The utilization of abundant ketones and aldehydes gives access to different substitution patterns, which allowed easy molecular engineering of the basic scaffold.

Cyclic voltammetry measurements of all new verdazyl radicals were performed, showing similar reversible oxidation and reduction processes as **V-(*i*Pr)$_2$-Ph**. Compound **V-(Ph)$_2$-Ph**, which represents the most electron deficient radical, showed the highest oxidation and reduction potentials and the lowest cell voltage of 1.45 V. In contrast, the all-alkyl variant **V-(Cy)$_2$-*t*Bu** represents the most electron-rich candidate, revealing a reversible oxidation and reduction at the lowest potentials and the highest cell voltage of 1.66 V. The properties of the other synthesized compounds are outlined in Figure 5. Overall, the cyclohexyl-substituted verdazyl radicals show the greatest cell potentials.

After confirming the bipolar properties of all verdazyl radicals in CV experiments, galvanostatic H-cell cycling was conducted to provide insights into the electrochemical stability of each verdazyl radical during oxidative cycling (Figure 6). Most striking within all performed H-cell measurements is the poor charge/discharge behavior of **V-(c4)$_2$-Ph**, which is consistent with its abovementioned limited air stability. **V-(Ph)$_2$-Ph** lacking any N-alkyl groups showed only moderate cycling stability, retaining about 60% of its initial capacity after 200 cycles. In both cases, the decomposition pathways seem to be more complex as compared to **V-(*i*Pr)$_2$-Ph**, as various decomposition products were observed. Among all tested compounds, the cyclohexyl-substituted verdazyl radicals showed an excellent cycling stability, with compounds of this series showing an even higher capacity retention as compared to the initially tested **V-(*i*Pr)$_2$-Ph**. Along these lines, **V-(Cy)$_2$-*t*Bu** showed the best cycling performance, retaining almost 95% capacity compared to its initial charging cycle. The lower cycling performance of **V-(Cy)$_2$-*p*OMePh** is likely attributed to clogging of the frit by the decomposition of the verdazyl radical during the reduction in the other side of the half-cell. In all cycling experiments, the CE during the cycling was excellent, averaging to greater than 99%.

For all compounds, TLC-MS analysis was conducted after each H-cell measurement. In the case of N-cyclohexyl verdazyls (**V-(Cy)$_2$-Ph**, **V-(Cy)$_2$-*t*Bu** and **V-(Cy)$_2$-*p*OMePh**), the dealkylated species could still be identified along with the corresponding intact verdazyl radical (see SI). However, when comparing

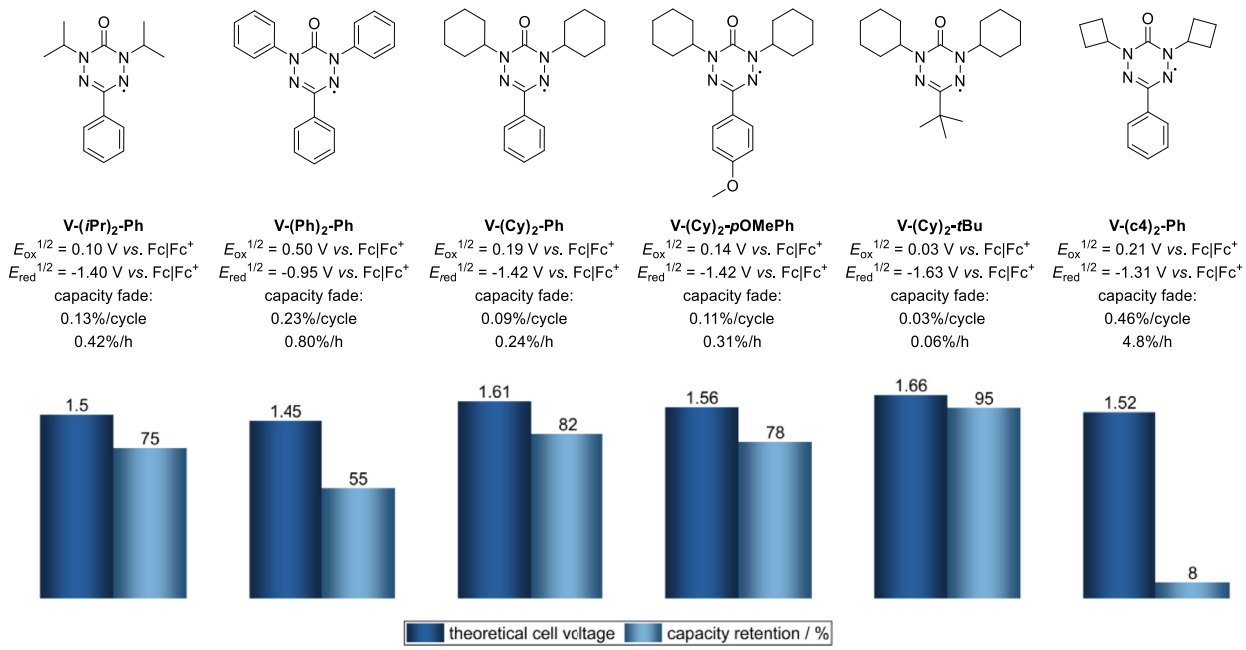

FIGURE 5 | Verdazyl radicals and the respective redox potentials. The capacity retention displays the remaining capacity after 200 charge/discharge cycles normalized to the first charging cycle and the theoretical cell voltage is given in V.

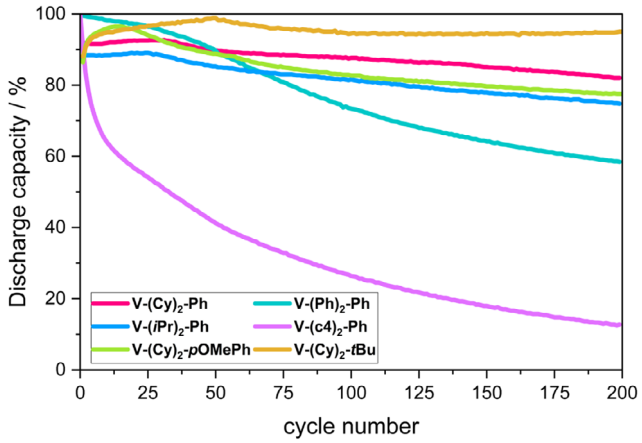

FIGURE 6 | Normalized discharge capacity against the initial charging cycle of all analogs. The cycling was performed at a constant current of 2 mA between the oxidized and neutral state of the molecule. The electrolyte solution consisted of 2.5 mM verdazyl radical and 0.1 M $TBAPF_6$ in MeCN. The H-cell was charged with 6.5 mL of electrolyte solution in both chambers.

the first and the last charging plots, the length of the plateau formed at lower potentials was significantly decreased, indicating a reduced decomposition compared to **V-(*i*Pr)$_2$-Ph** (Figure 7). Interestingly, for the most electron-rich verdazyl **V-(Cy)$_2$-*t*Bu**, the formation of the new plateau was less pronounced. This observation indicates that the decomposition product for **V-(Cy)$_2$-*t*Bu** is cycled at similar potentials as the corresponding verdazyl radical. A reason for this could be the already low oxidation potential of **V-(Cy)$_2$-*t*Bu**, as it is the most electron-rich ROM. When comparing the performances of **V-(Cy)$_2$-Ph** and **V-(Cy)$_2$-*p*OMePh**, the expected beneficial effect of the methoxy substituent was not observed. This outcome was further examined using DFT calculations on the cationic species formed from both radicals during oxidation. The calculations showed that the HOMO and LUMO surfaces as well as the electron densities and atomic charges of the tetrazine ring of both cations were similar, explaining the comparable cycling behavior (for details see SI). Overall, this analysis could show that the effect of the C-substituent on the performance of the verdazyl radical during oxidative cycling seems to be smaller compared to the N-substituent effect.

Taken together, the cyclohexyl-substituted verdazyl radicals delivered the most promising results in these cycling experiments. In addition to superior relative performance in terms of E_{cell}, the increased robustness renders them superior to the initially tested **V-(*i*Pr)$_2$-Ph**. To further probe their potential as bipolar molecules for symmetric RFBs, long-term stability during reductive cycling was examined by static galvanostatic cycling experiments over 200 charge/discharge cycles (Figure 8). Comparing the performance to the initially tested **V-(*i*Pr)$_2$-Ph**, **V-(Cy)$_2$-*p*OMePh** showed a lower performance by just retaining 38% of the capacity after 50 cycles. Interestingly, the more electron-rich radical **V-(Cy)$_2$-*t*Bu** outperforms **V-(Cy)$_2$-*p*OMePh**, suggesting that the instability during reductive cycling does not originate from the more electron-rich nature of the radical core but more likely from the instability arising from the charge destabilization of the negative charge through the electron-donating methoxy group on the aryl substituent. **V-(Cy)$_2$-Ph** and **V-(Cy)$_2$-*t*Bu**, which proved themselves the most promising candidates during oxidative cycling, also delivered the best performances during reductive cycling, also showing a significant improvement compared to the initially tested compound. While **V-(*i*Pr)$_2$-Ph** delivered moderate results, retaining 55% of its initial capacity after 200 cycles, the cyclohexyl-substituted verdazyl radicals also showed a high stability during cycling between their radical and anionic states. **V-(Cy)$_2$-Ph** retained about 83% of its initial cycling capacity, while **V-(Cy)$_2$-*t*Bu** retained 64% after 200 charge/

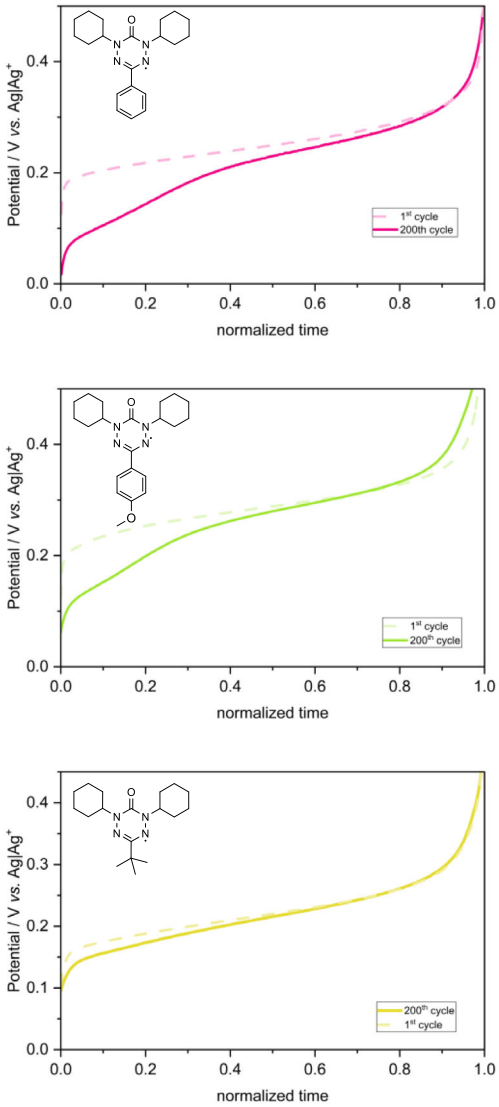

FIGURE 7 | Potential against time normalized against the total charging duration for the first and the last charging event of the corresponding compound (pink: V-$(Cy)_2$-Ph, green: **V-$(Cy)_2$-*p*OMePh**, yellow: **V-$(Cy)_2$-*t*Bu**).

discharge cycles. In both cases, the averaged Coulombic efficiency was greater than 99%. It has to be noted that in all cyclings, small deviations in the SOC were observed, which might also influence the results (see Figure S11–S20 in the SI for capacities normalized to the theoretical value) [28].

2.4 | Investigation of V-$(Cy)_2$-Ph as ROM in a Flow Battery

After optimizing the verdazyl scaffold through galvanostatic cycling in H-cells, the performance of the verdazyl radicals **V-$(Cy)_2$-Ph** and **V-$(Cy)_2$-*t*Bu** was evaluated in a nonaqueous RFB. The solubility of both compounds in MeCN was determined and found to be limited, with saturated solutions of only 28 mM for **V-$(Cy)_2$-Ph** and 49 mM for **V-$(Cy)_2$-*t*Bu**. In the presence of a supporting electrolyte, the solubility is expected to be even lower. Therefore, flow cycling experiments were conducted at a reduced concentration of 10 mM active material. To enhance the energy

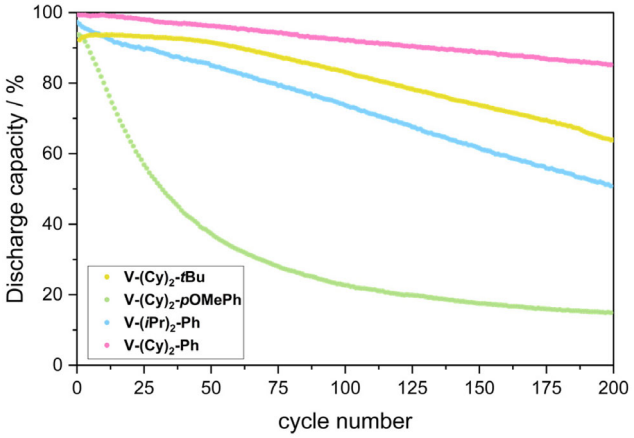

FIGURE 8 | Galvanostatic H-cell cyclings for reductive cycling of pink: **V-$(Cy)_2$-Ph**, green: **V-$(Cy)_2$-*p*OMePh**, yellow: **V-$(Cy)_2$-*t*Bu** and blue: **V-$(i\text{Pr})_2$-Ph**. Plotted is the discharge capacity normalized against the capacity of the first charging cycle over 200 charge/discharge cycles. The H-cell was loaded with 6.5 mL of the electrolyte in both chambers. The electrolyte solution consisted of 2.5 mM verdazyl and 0.1 M $TBAPF_6$ in MeCN and the constant current was set to −2 and 2 mA during charging and discharging, respectively.

density of the battery, potential strategies include increasing the solubility in organic solvents through the introduction of poly(-ethylene glycol) (PEG) chains or ionic functional groups (further strategies to improve the solubility of organic ROMs are discussed in the work by Byon et al.) [29]. The measurement was carried out using a minimally modified but not optimized RFB setup based on the Gen-2-Flow cell von Brushett et al. [24]. The electrodes (2.55 cm^2 geometric area) were composed of carbon paper (SIGRACET GDL 22 AA) and confined within compressible Teflon gaskets (GORE, 0.5 mm thickness). A Daramic-175 porous separator was used to separate the two half cells.

In both cyclings, a lot of active material was lost during the first cycle, with the capacity normalized to the theoretical capacity dropping from 96 to 82% for **V-$(Cy)_2$-Ph** and from 63 to 54% for **V-$(Cy)_2$-*t*Bu**. Unfortunately, the decay of the capacity was more pronounced than anticipated from the previous H-cell cycling. The discharge capacity of **V-$(Cy)_2$-*t*Bu** showed a decay of 0.34%/cycle (1.7%/h), whereas **V-$(Cy)_2$-Ph** showed a capacity decay of 0.74%/cycle and 2.7%/h. Notably, the lower capacity decay of **V-$(Cy)_2$-*t*Bu** might be attributed to the already lower SOC in the first cycle, as **V-$(Cy)_2$-*t*Bu** started utilizing 63% of active material, whereas **V-$(Cy)_2$-Ph** started at 96% SOC. Despite the low capacity retention, the systems exhibited good electrochemical efficiencies. The Coulombic efficiency remained stable slightly above 80% throughout cycling, and voltage efficiencies of 94% for **V-$(Cy)_2$-Ph** and 91% for **V(Cy)tBu** were obtained. In both cases, the anticipated positive effect of alkyl substitution on the operating potential could be confirmed. Average cell voltages of 1.56 V for **V-$(Cy)_2$-Ph** and 1.61 V for **V-$(Cy)_2$-*t*Bu** were observed during charge–discharge cycling, exceeding those of previously reported high-voltage oxo-verdazyls [19]. The higher cell voltage of the all-alkyl verdazyl radical **V-$(Cy)_2$-*t*Bu** is also consistent with prior cyclic voltammetry studies. Small deviations from the theoretical cell voltages are attributed to polarization effects and the molecular decomposition discussed in this work, which lead to voltage losses under

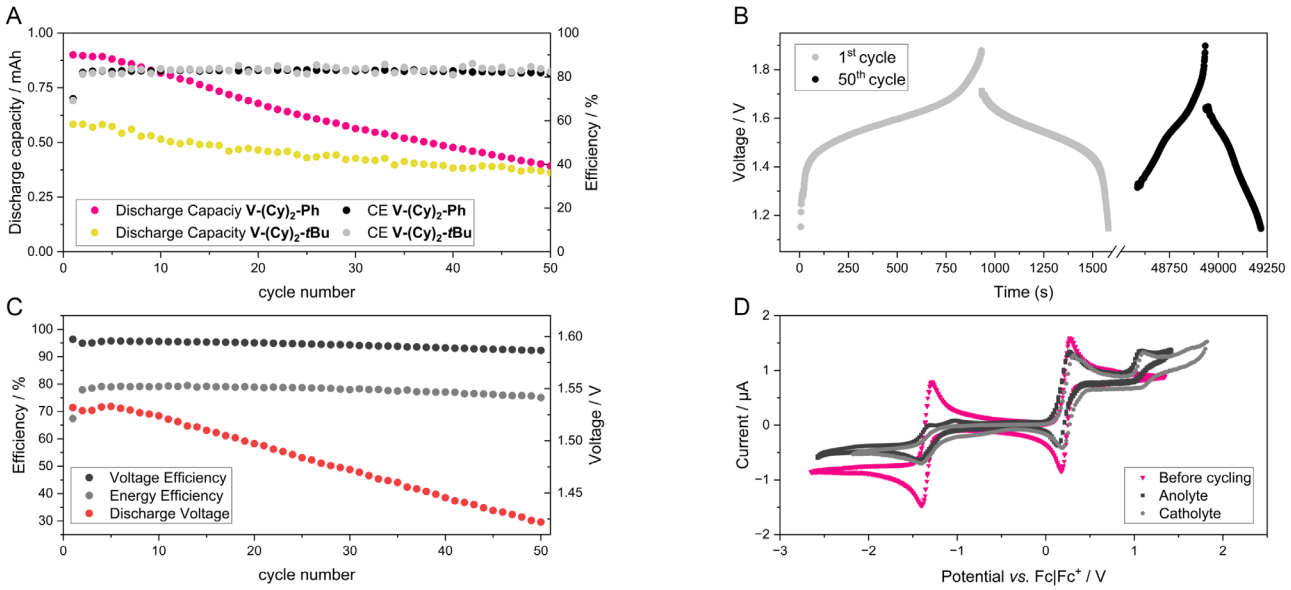

FIGURE 9 | Galvanostatic cycling of **V-(Cy)$_2$-Ph** (9.6 mM) and **V-(Cy)$_2$-*t*Bu** (10 mM) in MeCN/ $TBAPF_6$ (0.1 M), 5 mA (1.96 mA/cm^2, 0.18 C-rate) over 50 charge–discharge cycles. (A) discharge capacities (mAh) and the Coulombic efficiencies (%) over 50 charge/discharge cycles (B) cell voltage against time for the first and last charge–discharge cycle of **V-(Cy)$_2$-Ph** (C) voltage- and energy efficiency and averaged discharge voltage against the cycle number of **V-(Cy)$_2$-Ph** (D) CV analysis of pre- and postcycling electrolyte solutions of **V-(Cy)$_2$-Ph**.

flow cell operation. Examination of the potential–time profiles reveals a newly formed and well-defined plateau for **V-(Cy)$_2$-Ph**, resulting in a shift of the overall charge/discharge potentials from 1.59/1.53 V to 1.54/1.42 V (Figure 9C). In agreement to this apparent new redox-active species is the appearance of a new reversible redox peak detected in postcycling CV measurements (Figure 9D). As these observations were consistent with earlier H-cell results (see Figure 7), we performed TLC mass analysis of the residual electrolyte and were able to confirm the appearance of the decomposition product in both anolyte and catholyte. In parallel, we conducted impedance spectroscopy before the first and after the last cycle to rule out any performance loss due to membrane clogging. Since no significant changes in the resistance could be observed, suggesting that no major membrane clogging occurred (see SI).

As already mentioned, the capacity fade was more pronounced under flow conditions than in H-cells. Attempts to increase the performance through polarity reversals were not successful (see SI Figure S26). This accelerated decline may be attributed to faster crossover of active species through the porous separator, allowing the decomposition product to migrate to the reductive side of the battery. The presence of protons in the anolyte half-cell may have compromised the reversibility of the redox processes. This would also explain why CV measurements of the electrolytes anolyte catholyte tank result in nearly identical CV curves, indicating mixing of the two electrolyte solutions. Also, the irreversibility of the reduction peak can be attributed to the presence of protons. The utilization of a porous standard separator during the flow cycling could have led to an insufficient separation of the electrolytes, causing the more rapid capacity decay. DFT calculations suggest that the crossover, caused by the high porosity of the separator, can also accelerate the degradation of the verdazyl through the previously discussed Hofmann-type elimination (see SI for details). This represents a major limitation of the bipolar ROM investigated here, as one of the key advantages of symmetric RFB systems is that mixing of oxidized and reduced species should result only in self-discharge rather than irreversible decomposition. Improving the selectivity and compatibility by using more sophisticated membranes could mitigate this effect and improve overall performance.

The flow cell cycling demonstrates that the previously discussed decomposition still limits the applicability of the verdazyl radical in symmetric RFBs, since it is clearly showing the incompatibility between anionic and cationic species. Nevertheless, the results confirm that the targeted voltage increase was successfully achieved through the introduction of alkyl substituents.

3 | Conclusion

In this work, the long-term stability during battery cycling of various synthesized *N*,*N*'-dialkylated verdazyl radicals was investigated. With a higher theoretical cell voltage than other stable radicals in its class, they represent a promising candidate for charge-storage materials in RFBs. Long-term stability tests of *N*,*N*'-diisopropyl verdazyl radicals revealed the formation of a decomposition product during cycling between the neutral and cationic states. This decomposition product has been identified as the dealkylated verdazyl radical formed through loss of propene. Fortunately, upon protonation the dealkylated verdazyl radical can take part in the cycling of the battery so that the overall amount of active material is not decreasing. While the formation of the new species is not reducing the overall capacity of the battery, the decomposition results in a small loss of cell voltage and an asymmetric battery setup. Moreover, the gas evolution associated with the decomposition could lead to problems with respect to the cell setup. To circumvent this, *N*,*N*'-dicyclohexyl verdazyl radicals were synthesized and delivered improved results regarding the discussed decomposition. **V-(Cy)$_2$-Ph**

and **V-(Cy)$_2$-*t*Bu** showed very promising results for both oxidation and reduction, retaining over 80% of their initial charging capacity after 200 cycles in H-cells. Since for **V-(Cy)$_2$-*p*OMePh** the negative charge during reductive cycling was tremendously destabilized, only **V-(Cy)$_2$-Ph** and **V-(Cy)$_2$-*t*Bu** were tested under flow conditions. The capacity fade for both molecules was more severe compared to the H-cell cycling, with **V-(Cy)$_2$-Ph** retaining 30% and V-(Cy)$_2$-*t*Bu 27% of the theoretical capacity after 50 cycles. Despite the rather low stability, the envisioned positive effect of alkyl substitution on the operating potential could be confirmed with an average cell potential of 1.56 V for **V-(Cy)$_2$-Ph** and 1.61 V for **V-(Cy)$_2$-*t*Bu**. These results demonstrate that alkylated verdazyl radicals possess considerable potential as redox-active materials. To improve these compounds viability in RFBs, future work should focus on membrane optimization within the redox flow cell setup. Furthermore, the synthetic accessibility of a broader variety of N-alkylated verdazyl radicals needs to be improved, since the introduction of bulkier groups has not yet been achieved.

Author Contributions

Elena S. Horst: conceptualization (lead); data curation (lead); investigation (lead); writing – original draft (equal). **Karin Sowa**: conceptualization (lead); data curation (lead); investigation (lead); writing – original draft (equal). **Lena Lezius**: writing – review & editing (supporting). **Nick Fehlings**: data curation (equal); methodology (equal). **Constantin Daniliuc**: data curation (equal); methodology (equal); validation (supporting); writing – review & editing (supporting). **Sascha Nowak**: data curation (equal); methodology (equal); supervision (supporting). **Mariano Grünebaum**: supervision (equal); writing – review & editing (supporting). **Martin Winter**: formal analysis (equal); funding acquisition (equal); validation (equal); writing – review & editing (equal).

Acknowledgments

This work was supported by the Deutsche Forschungsgemeinschaft (GRK 2678-437785492), the Fonds der Chemischen Industrie (Ph.D. fellowship to L.L. and E.S.H.) and the Ministry for Culture and Science of North Rhine Westphalia, Germany for funding the International Graduate School for Battery Chemistry, Characterization, Analysis, Recycling and Application (BACCARA, K.S.). The authors gratefully thank Lasse Schröder, Katja Zembsch and Jana Lohmann (all WWU), and Nicolas Daub (TU Eindhoven) for helpful discussions and experimental support.

Open access publishing facilitated by Universita degli Studi di Parma, as part of the Wiley - CRUI-CARE agreement.

Funding

This study was supported by Deutsche Forschungsgemeinschaft (GRK 2678-437785492), Ministerium für Innovation, Wissenschaft und Forschung des Landes Nordrhein-Westfalen.

Conflicts of Interest

The authors declare no conflicts of interest.

Data Availability Statement

The data that support the findings of this study are available in the supplementary material of this article.

References

1. F. Creutzig, C. Breyer, J. Hilaire, J. Minx, G. P. Peters, and R. Socolow, "The Mutual Dependence of Negative Emission Technologies and Energy Systems," *Energy & Environmental Science* 12 (2019): 1805–1817.

2. Q. Hassan, P. Viktor, T. J. Al-Musawi, et al., "The Renewable Energy Role in the Global Energy Transformations," *Renewable Energy Focus* 48 (2024): 100545.

3. B. Dunn, H. Kamath, and J.-M. Tarascon, "Electrical Energy Storage for the Grid: A Battery of Choices," *Science* 334 (2011): 928–935.

4. W. Wang, Q. Luo, B. Li, X. Wei, L. Li, and Z. Yang, "Recent Progress in Redox Flow Battery Research and Development," *Advanced Functional Materials* 23 (2013): 970–986.

5. C. R. Peltier, Z. Rhodes, A. J. Macbeth, et al., "Suppressing Crossover in Nonaqueous Redox Flow Batteries with Polyethylene-Based Anion-Exchange Membranes," *ACS Energy Letters* 7 (2022): 4118–4128.

6. S. E. Doris, A. L. Ward, A. Baskin, et al., "Macromolecular Design Strategies for Preventing Active-Material Crossover in Non-Aqueous All-Organic Redox-Flow Batteries," *Angewandte Chemie International Edition* 56 (2017): 1595–1599.

7. K. H. Hendriks, S. G. Robinson, M. N. Braten, et al., "High-Performance Oligomeric Catholytes for Effective Macromolecular Separation in Nonaqueous Redox Flow Batteries," *ACS Central Science* 4 (2018): 189–196.

8. M. J. Baran, M. N. Braten, E. C. Montoto, et al., "Designing Redox-Active Oligomers for Crossover-Free, Nonaqueous Redox-Flow Batteries with High Volumetric Energy Density," *Chemistry of Materials : A Publication of the American Chemical Society* 30 (2018): 3861–3866.

9. J. S. Tracy, E. S. Horst, V. A. Roytman, and F. D. Toste, "Development of High-Voltage Bipolar Redox-Active Organic Molecules through the Electronic Coupling of Catholyte and Anolyte Structures," *Chemical Science* 13 (2022): 10806–10814.

10. R. A. Potash, J. R. McKone, S. Conte, and H. D. Abruña, "On the Benefits of a Symmetric Redox Flow Battery," *Journal of the Electrochemical Society* 163 (2016): A338–A344.

11. M. A. Raihan and C. A. Dyker, "Status and Prospects for Symmetric Organic Redox Flow Batteries," *Journal of Energy Chemistry* 100 (2025): 125–143.

12. M. Li, J. Case, and S. D. Minteer, "Bipolar Redox-Active Molecules in Non-Aqueous Organic Redox Flow Batteries: Status and Challenges," *ChemElectroChem* 8 (2021): 1215–1232.

13. L. Wylie, T. Blesch, R. Freeman, et al., "Reversible Reduction of the TEMPO Radical: One Step Closer to an All-Organic Redox Flow Battery," *ACS Sustainable Chemistry & Engineering* 8 (2020): 17988–17996.

14. T. Hagemann, J. Winsberg, B. Häupler, et al., "A Bipolar Nitronyl Nitroxide Small Molecule for an All-Organic Symmetric Redox-Flow Battery," *NPG Asia Materials* 9 (2017): e340–e340.

15. B. I. Loomans, S. E. Bottle, and J. P. Blinco, "Bipolar Isoindoline Nitroxide for Nonaqueous Symmetrical Redox Flow Battery," *Batteries & Supercaps* 6 (2023): e202200561.

16. S. Mujahed, J. Janabel, K. Shaw, R. Cagliani, and T. Amatov, "Nitrogen-Centered Organic Persistent Radicals Catalyze Redox-Neutral C—C Bond Forming Reactions," *Angewandte Chemie International Edition* 64 (2025): e202511233.

17. G. D. Charlton, S. M. Barbon, J. B. Gilroy, and C. A. Dyker, "A Bipolar Verdazyl Radical for a Symmetric All-Organic Redox Flow-Type Battery," *Journal of Energy Chemistry* 34 (2019): 52–56.

18. J. S. Steen, F. De Vries, J. Hjelm, and E. Otten, "Bipolar Verdazyl Radicals for Symmetrical Batteries: Properties and Stability in All States of Charge," *Chemphyschem : A European Journal of Chemical Physics and Physical Chemistry* 24 (2023): e202200779.

19. A. Korshunov, M. J. Milner, M. Grünebaum, A. Studer, M. Winter, and I. Cekic-Laskovic, "An Oxo-Verdazyl Radical for a Symmetrical Non-Aqueous Redox Flow Battery," *Journal of Materials Chemistry A* 8 (2020): 22280–22291.

20. J. S. Steen, J. L. Nuismer, V. Eiva, et al., "Blatter Radicals as Bipolar Materials for Symmetrical Redox-Flow Batteries," *Journal of the American Chemical Society* 144 (2022): 5051–5058.

21. E. C. Paré, D. J. R. Brook, A. Brieger, M. Badik, and M. Schinke, "Synthesis of 1,5-Diisopropyl Substituted 6-Oxoverdazyls," *Organic & Biomolecular Chemistry* 3 (2005): 4258.

22. J. B. Gilroy, S. D. J. McKinnon, B. D. Koivisto, and R. G. Hicks, "Electrochemical Studies of Verdazyl Radicals," *Organic Letters* 9 (2007): 4837–4840.

23. B. J. Neyhouse and F. R. Brushett, In*Encyclopedia of Energy Storage* (Elsevier, 2022) pp. 453–465.

24. J. D. Milshtein, K. M. Tenny, J. L. Barton, J. Drake, R. M. Darling, and F. R. Brushett, "Quantifying Mass Transfer Rates in Redox Flow Batteries," *Journal of the Electrochemical Society* 164 (2017): E3265–E3275.

25. Deposition numbers 2481893 (for V-(iPr)-Ph) and 2481894 (for V-(c4) 2-Ph) contain the supplementary crystallographic data for this paper. These data are provided free of charge by the joint Cambridge Crystallographic Data Centre and Fachinformationszentrum Karlsruhe Access Structures service.

26. F. A. Neugebauer, H. Fischer, and R. Siegel, "6-Oxo- Und 6-Thioxoverdazyle," *Chemische Berichte* 121 (1988): 815–822.

27. N. M. Saji, M. R. Taylor, D. M. Mazzucato, et al., "Synthesis, Structure, and Redox Properties of Nonsymmetric 6-Oxoverdazyls," *Organic Letters* 26 (2024): 8696–8701.

28. M.-A. Goulet, L. Tong, D. A. Pollack, et al., "Extending the Lifetime of Organic Flow Batteries via Redox State Management," *Journal of the American Chemical Society* 141 (2019): 8014–8019.

29. V. Singh and H. R. Byon, "Solubility and Stability of Redox-Active Organic Molecules in Redox Flow Batteries," *ACS Applied Energy Materials* 7 (2024): 7562–7575.

Supporting Information

Additional supporting information can be found online in the Supporting Information section. **Supporting Fig. S1**: CV scan of V-(iPr)2-Ph (2.5 mM) in 0.1 M TBAPF6 /MeCN at a scan rate of 100 mV/s. **Supporting Fig. S2**: CV scan of V-(Cy)2-pOMePh (2.5 mM) in 0.1 M TBAPF6 /MeCN at a scan rate of 100 mV/s. **Supporting Fig. S3**: CV scan of V-(Cy)2-Ph (2.5 mM) in 0.1 M TBAPF6 /MeCN at a scan rate of 100 mV/s. **Supporting Fig. S4**: CV scan of V-(Ph)2-Ph (2.5 mM) in 0.1 M TBAPF6 /MeCN at a scan rate of 100 mV/s. **Supporting Fig. S5**: CV scan of V-(Cy)2-tBu (2.5 mM) in 0.1 M TBAPF6 /MeCN at a scan rate of 100 mV/s. **Supporting Fig. S6**: CV scan of V-(c4)2-Ph (2.5 mM) in 0.1 M TBAPF6 /MeCN at a scan rate of 100 mV/s. **Supporting Fig. S7**: Cyclic voltammetry measurements of V-(Cy)2-tBu and V-(Cy)2-Ph at scan rates ranging from 50 to 400 mV/s. **Supporting Fig. S8**: Current density j against scan rate0.5 for V-(Cy)2-Ph (right) and V-(Cy)2-tBu (right). **Supporting Fig. S9**: Nicholson parameter vs scan rate for scan rate0.5 for V-(Cy)2-Ph (right) and V-(Cy)2-tBu (right). **Supporting Fig. S10**: Customized Setup for H-cell cycling. **Supporting Fig. S11**: H-Cell cycling of V-(Cy)2-tBu/V-(Cy)2-tBu+ (2.5 mM) in 0.1 M TBAFPF6 / MeCN at a current of 2 mA. **Supporting Fig. S12**: H-Cell cycling of V-(Cy)2-pOMePh/V-(Cy)2-pOMePh+ (2.5 mM) in 0.1 M TBAFPF6 / MeCN at a current of 2 mA. **Supporting Fig. S13**: H-Cell cycling of V-(iPr)2-Ph/V-(iPr)2-Ph+ (2.5 mM) in 0.1 M TBAFPF6/MeCN at a current of 2 mA. **Supporting Fig. S14**: H-Cell cycling of V-(Cy)2-Ph/V-(Cy)2-Ph+ (2.5 mM) in 0.1 M TBAFPF6/MeCN at a current of 2 mA. **Supporting Fig. S15**: H-Cell cycling of V-(Ph)2-Ph/V-(Ph)2-Ph+ (2.5 mM) in 0.1 M TBAFPF6 / MeCN at a current of 2 mA. **Supporting Fig. S16**: H-Cell cycling of V-(c4)2-Ph/V-(c4)2-Ph+ (2.5 mM) in 0.1 M TBAFPF6 / MeCN at a current of 2 mA. **Supporting Fig. S17**: H-Cell cycling of V-(iPr)2-Ph-/V-(iPr)2-Ph (2.5 mM) in 0.1 M TBAFPF6/MeCN at a current of 2 mA. **Supporting Fig. S18**: H-Cell cycling of V-(Cy)2-Ph-/V-(Cy)2-Ph (2.5 mM) in 0.1 M TBAFPF6 / MeCN at a current of 2 mA. **Supporting Fig. S19**: H-Cell cycling of V-(Cy)2-tBu-/V-(Cy)2-tBu (2.5 mM) in 0.1 M TBAFPF6 / MeCN at a current of 2 mA. **Supporting Fig. S20**: H-Cell cycling of V-(Cy)2-pOMePh-/ V-(Cy)2-pOMePh (2.5 mM) in 0.1 M TBAFPF6 / MeCN at a current of 2 mA. **Supporting Fig. S21**: Example of the preparation for after cycling TLC analysis after oxidative cycling. **Supporting Fig. S22**: Chromatogram and mass spectrum taken of the headspace after oxidative cycling. **Supporting Fig. S23**: TLC after 200 charge discharge cycles of V-(iPr)2-Ph-/V-(iPr)2-Ph. **Supporting Fig. S24**: Used electrochemical cell (Gen 2-Flow cell). **Supporting Fig. S25**: Additional data for the flow cycling of V-(Cy)2-tBu: Left: Efficiencies plotted against the cycle number; Middel: cell potential against time for the first and last chare/discharge cycle; Right: CV-measurements taken of the electrolyte before and after the cycling. **Supporting Fig. S26**: Discharge capacity and coulombic efficiency of V-(Cy)2-Ph during flow cycling with polarity reversals. **Supporting Fig. S27**: Nyquist plot of V-(Cy)2-Ph-/V-(Cy)2-Ph (9.6 mM) in 0.1 M TBAPF6 prior and after cycling. Data was collected using the Metrohm Autolab B.V. M204 potentiostat. **Supporting Fig. S28**: a) HOMO surface, b) LUMO surface (isovalues 0.02) and c) electron density (isovalue = 0.3) of V (Cy)2-Ph+. **Supporting Fig. S29**: a) HOMO surface, b) LUMO surface (isovalues 0.02) and c) electron density (isovalue = 0.3) of V (Cy)2-pOMePh+. **Supporting Fig. S30**: Crystal structure of compound V-(iPr)-Ph. Figure S30. Crystal structure of compound V-(iPr)-Ph. **Supporting Fig. S31**: Crystal structure of compound V-(c4)2-Ph. **Supporting Fig. S32**: Crystal structure of compound V-(c4)-O-Ph. **Supporting Table 1**: Crystal data and structure refinement for V-(c4)-O-Ph.